Nanoscale

PAPER

View Article Online
View Journal

Cite this: DOI: 10.1039/d5nr05417f

Pressure-induced phase transition on layered $HgPSe_3$ revealed by optical, structural and vibrational studies

Beatriz de Simoni, *†[a] Robert Oliva, †[b] Miłosz Rybak, [a] Jan Kopaczek, [a] Agata K. Tołłoczko, [a] Jordi Ibañez, [b] Filip Dybała, [a] Paweł Scharoch, [a] Iva Plutnarová, [c] Zdeněk Sofer, [c] Óscar Gomis, [d] Pablo Botella, [e] Daniel Errandonea, [e] Nikolas Antonatos *[a] and Robert Kudrawiec [a]

The family of transition metal phosphorus trichalcogenides (MPX_3, where M is a transition metal and X = S or Se) has recently attracted considerable attention due to their tunable band gaps and synergistic effects among electronic, magnetic, structural, and optical properties. We examine the influence of hydrostatic pressure on the optical, structural and vibrational properties of layered $HgPSe_3$ through spectroscopic and diffraction techniques combined with first-principles calculations. Optical absorption measurements reveal a phase transition at 3.6 GPa, evidenced by a decrease in the band gap energy of approximately 200 meV, resulting in a change in sample color from bright to dark red. The same phase transition was confirmed by structural methods: powder X-ray diffraction and Raman spectroscopy. We propose that the compound undergoes a structural transition from its ambient pressure monoclinic phase to a high-pressure triclinic phase. Birch–Murnaghan fits give an experimental bulk modulus of B_0 = 29.7 GPa, in very good agreement with the theoretical value of B_0 = 28.1 GPa. Experimental pressure coefficients are obtained and compared with theoretical predictions. Our findings unveil a complex interplay between the structural and optical properties of $HgPSe_3$ under pressure, which could be exploited to fabricate novel applications based on the tunable properties of van der Waals materials.

Received 23rd December 2025,
Accepted 16th March 2026

DOI: 10.1039/d5nr05417f

rsc.li/nanoscale

1 Introduction

Following the breakthrough success of the isolation of atomically thin graphene,[1] layered materials with sizable band gaps have become highly sought after. For instance, group VI transition metal dichalcogenides (TMDs), such as MoS_2, $MoSe_2$, WS_2 and WSe_2, demonstrate strong excitonic, valleytronic, and spintronic properties.[2–10] In search of additional degrees of freedom, another family of 2D materials, the transition-metal phosphorus trichalcogenides (TMPTs) with a chemical formula of MPX_3 (where X = S, Se), has attracted special interest due to their intrinsic magnetic properties. The relatively large band gaps of TMPTs, ranging from 1.3 to 3.5 eV,[11] make them efficient light absorbers, well-suited for applications across a broad wavelength spectrum. These materials have therefore become the subject of research in different fields covering areas such as optoelectronics, intercalation chemistry and electrocatalysis.[12–16] With a band gap of approximately 2 eV at ambient conditions, $HgPSe_3$ has been utilized as a photodetector exhibiting a broad spectral sensitivity, spanning from X-rays to visible light, which was later found to show an ultrafast photoresponse in the order of nanoseconds.[17,18]

Under ambient conditions, transition metal thiophosphates MPS_3 exhibit a monoclinic structure (space group, s.g. $C2/m$), with the exception of $HgPS_3$, which is triclinic $P\bar{1}$, while most selenide counterparts ($MPSe_3$ for which M = Mn, Fe, Cd, Zn, Mg) have a rhombohedral structure (space group $R\bar{3}$).[19–22] Notably, $HgPSe_3$ belongs to the monoclinic system as do most MPS_3 compounds and $NiPSe_3$, although with different stacking (ABAB, as opposed to AAA) and space group ($C2/c$ as opposed to $C2/m$).[23,24] Hence, the widely explored MPX_3 compounds can serve as a benchmark to better understand the physical properties and potential applicability of $HgPSe_3$, both of which remain largely unexplored in the literature.

[a]Department of Semiconductor Materials Engineering, Wroclaw University of Science and Technology, Wybrzeże Wyspiańskiego 27, 50-370 Wrocław, Poland. E-mail: beatriz.desimoni@pwr.edu.pl, nikolaos.antonatos@pwr.edu.pl
[b]Geosciences Barcelona (geo3bcn-CSIC), C/Lluís Solé i Sabarís s/n, 08028 Barcelona, Catalonia, Spain
[c]Department of Inorganic Chemistry, University of Chemistry and Technology Prague, Technická 5, 166 28 Prague 6, Czech Republic
[d]Centro de Tecnologías Físicas, MALTA Consolider Team, Universitat Politècnica de València, 46022 València, Spain
[e]Department of Applied Physics ICMUV, MALTA Consolider Team, Universitat de València, 46100 Valencia, Spain
† These authors contributed equally to this work.

Similar to the changes observed in the optical, magnetic, and electronic properties of van der Waals crystals when their thickness is reduced to the monolayer limit, the application of hydrostatic pressure to the bulk material decreases the interlayer spacing and strengthens interlayer interactions, which may lead to different emergent phenomena, such as metallization, Mott metal–insulator transition, spin crossover and structural phase transition.[25–32] For example, it is well known that the band gap of MoS_2 evolves from indirect in bulk form to direct in the monolayer limit, accompanied by an increase in band gap energy from approximately 1.3 to 1.9 eV,[2] which makes it a promising material for optoelectronics applications.[4] Interestingly, applying hydrostatic pressure to monolayer MoS_2 revealed direct–indirect gap crossover.[33] For the case of bulk materials, pressure-induced band gap crossover has been observed, for instance in $CrPS_4$ (which also lies in the monoclinic $C2/m$ structure) and III–VI layered compounds.[34,35] Therefore, hydrostatic pressure is a powerful tool for probing the nature of optical transitions, offering valuable insights into the electronic band structure.[36]

In this work, we investigate the high-pressure behavior of $HgPSe_3$ at room temperature using optical absorption spectroscopy, as well as powder X-ray diffraction (XRD) and Raman spectroscopy. The pressure coefficients and bulk moduli were obtained. All the employed experimental techniques evidence a phase transition of electronic and structural nature, suggesting a quasi-direct to indirect band gap crossover accompanied by a monoclinic to triclinic structural transition. The experimental results are compared with theoretical predictions obtained within the density functional theory (DFT) framework, which provides the lattice parameters, electronic band structure and phonon dispersion curves of the low-pressure phase of $HgPSe_3$.

2 Methods

2.1 Synthesis of $HgPSe_3$

$HgPSe_3$ samples were grown by chemical vapor transport (CVT) using HgI_2 as a transport agent. The elements were sealed under vacuum in a quartz ampoule and subjected to a controlled temperature gradient, enabling material transport in the vapor phase and subsequent crystal growth at the cooler end. The crystal structure of TMPTs consists of layers of $(P_2Se_6)^{4-}$ clusters stabilized by the divalent metal cations M^{2+} and held together by weak van der Waals (vdW) interactions, while the in-plane atoms are strongly joined by covalent bonds (see Fig. 1).[37] Detailed information on the synthesis and characterization of $HgPSe_3$ has been reported elsewhere.[17]

2.2 High-pressure optical absorption

The diamond anvil cell (DAC) technique was employed to measure optical absorption with hydrostatic pressure dependence. This cell is composed of two diamonds with flat tips (culets, with diameter of 450 μm) facing each other, and a metal disk (gasket) between them to prevent the diamonds from touching each other. A 150 μm diameter hole is drilled in the center of the gasket to form the sample chamber. This cavity hosted the sample and a pressure-transmitting medium (Daphne 7575), which is chemically inert and has desirable optical transparency, ensuring quasi-hydrostatic conditions. A ruby microsphere was included for pressure calibration *via* the ruby fluorescence technique.[39] The ruby emission was collected with an Avantes spectrometer (655–755 nm). The larger surface of the diamonds is attached to backing plates that allows optical access, and the whole structure is held inside a piston-cylinder device. The piston exerts pressure through a metallic inflatable membrane.[40] A halogen lamp was utilized to probe the sample. The transmitted light passed through a 50× microscope objective and was collected with a wide-range spectrometer (StellarNet spectrometer 300–1100 nm). All measurements were performed at room temperature. The same setup was used to collect optical images, simply by replacing the spectrometer with a CCD camera.

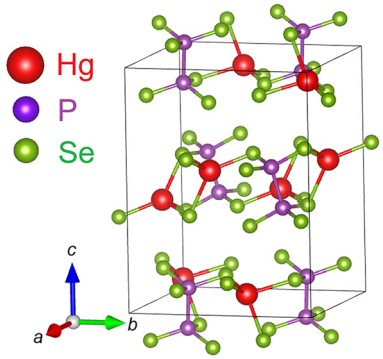

Fig. 1 Crystal structure of $HgPSe_3$ at ambient conditions (s.g. 15, $C2/c$). Red balls represent Hg atoms, while green and purple represent Se and P, respectively. This figure was created from PDF card 00-031-0858 using VESTA.[38]

2.3 High-pressure photoluminescence

Photoluminescence (PL) spectroscopy was carried out using a custom-built optical system equipped with a 550 mm focal-length grating monochromator (Horiba Jobin Yvon iHR 550) and a multichannel liquid nitrogen-cooled Si CCD array detector. The sample was excited using a continuous-wave 532 nm laser with an incident power of 100 μW. The laser beam was focused using a 50× objective lens (NA = 0.55). The procedure used to obtain high hydrostatic pressure was the same as in the case of optical absorption measurements. The sample was mounted inside a DAC, together with a ruby sphere used for pressure calibration. Daphne 7575 was used as pressure-transmitting medium. Measurements were performed at room temperature.

2.4 High-pressure Raman spectroscopy

A single flake of $HgPSe_3$ was loaded in a gasketed membrane-type DAC with 400 μm culet-size diamonds. A mixture of methanol–ethanol–water (16 : 3 : 1) was employed as pressure-

transmitting medium, and the ruby fluorescence method was used to determine the pressure. The 514.5 nm laser line of an Ar^+ laser was used as excitation source at a power lower than 10 mW in order not to damage the sample. Unpolarized, back-scattering confocal micro-Raman measurements were acquired using a 50× objective that collected the scattered light into a Jobin–Yvon T64000 spectrometer using the double-subtractive configuration to access a low wavenumber spectral window down to Raman shifts of ≈15 cm^{-1} acquired with a liquid N_2-cooled CCD camera, which allowed for detection of the low-frequency modes involving Se and Hg atoms. Due to the sample's fragility to light at ambient pressure, the corresponding spectrum was recorded in macroscopic configuration using a laser power lower than 4 mW on a spot of 250 μm in diameter.

2.5 High-pressure X-ray diffraction

High-pressure angle-dispersive powder X-ray diffraction measurements were acquired at room temperature at the BL04-MSPD beamline in ALBA synchrotron facility.[41] XRD experiments were performed with a wavelength of 0.4246 Å. The sample, which had been ground into fine powder in an ethanol bath, was loaded with a copper flake in a DAC with 400 μm-diameter diamond culets. A mixture of methanol–ethanol–water (16 : 3 : 1) was used as pressure-transmitting medium and the applied pressure was determined with the equation of state (EoS) of copper.[42] The sample-to-detector distance (≈240 mm) was determined fitting a LaB_6 calibrant with the DIOPTAS program.[43] The experimental lattice parameters were obtained as a function of pressure using the DICVOL and FullProf packages.[44–46]

Before concluding the Experimental section, we briefly address the pressure-transmitting media used in this study. Optical absorption measurements were performed using Daphne 7575, whereas Raman spectroscopy and X-ray diffraction experiments were carried out with a methanol–ethanol–water (16 : 3 : 1) mixture. Daphne 7575 provides quasi-hydrostatic conditions up to 6.5 GPa, and the pressure standard deviation within the DAC is as low as 0.08 GPa at 8 GPa—the maximum pressure reached in our experiments. The methanol–ethanol–water mixture remains quasi-hydrostatic up to 10 GPa.[47] Therefore, both pressure media ensure comparable quasi-hydrostatic conditions throughout the investigated pressure range. Moreover, to verify reversibility, decompression data were collected for all experimental techniques and are available in Fig. S1–S4 from the SI.

2.6 Computational details

DFT calculations have been performed using the Vienna *Ab Initio* Simulation Package (VASP).[48] The electron–ion interaction was modeled using projector-augmented-wave technique.[49] The Perdew–Burke–Ernzerhof (PBE) exchange–correlation (XC) functional was employed.[50] A plane-wave basis cutoff energy of 600 eV and a 12 × 6 × 6 Monkhorst–Pack *k*-point grid for the Brillouin Zone (BZ) integrations were set.[51] These values ensured convergence of the lattice constants and the electronic gaps were within precision of 0.001 Å and 0.001 eV, respectively. A Gaussian smearing of 0.02 eV was used for integration in reciprocal space. The semi-empirical Grimme's correction with Becke–Johnson damping (D3-BJ) was employed to properly describe the weak vdW forces.[52] The spin–orbit (SO) interaction was taken into account. To obtain the phonon dispersion relations, the finite-differences approach was employed,[53,54] as implemented in the Phonopy v 2.44.0 package.[55] For the purpose of phonon calculations, the atomic positions were re-optimized until the residual forces on all atoms were smaller than 10^{-5} eV $Å^{-1}$. The calculations were carried out using a 2 × 2 × 1 supercell containing 160 atoms. These ensured that all phononic branches exhibited non-imaginary energies. The Hellmann–Feynman forces were extracted from a set of symmetry-inequivalent atomic displacements, and the resulting force constants were used to construct the dynamical matrices and compute the phonon dispersion.

3 Results and discussion

3.1 Optical properties

Room-temperature optical absorption measurements up to 8.4 GPa were acquired and the spectra are shown in Fig. 2a. It can be seen that the absorption edge shifts to lower energies as pressure increases, and a phase transition is evidenced at approximately 3.6 GPa, which is marked by a drop of $\Delta E \approx$ 200 meV in the absorption edge energy and accompanied by a change in slope of the absorption coefficient curves. At low pressures, the absorption spectra exhibit the characteristic shape of a direct transition (see left inset of Fig. 2b). With increasing pressure, no significant changes in the line shape are observed in the spectra up to 3.6 GPa. Above this threshold, however, the absorption edge becomes progressively smoother, and the spectral shape evolves towards that of an indirect transition (see right inset of Fig. 2b).

A reasonable explanation for the change in slope of the absorption spectra at pressure values above 3.6 GPa is that the band gap becomes indirect, which is the case for other layered semiconductors such as SnP_2S_6 and $CrPS_4$.[35,56] The assumption of change in band gap nature from quasi-direct to indirect is supported by room temperature pressure-dependent photoluminescence measurements presented in Fig. S5 (SI). With increasing pressure, the emission energies shift to lower values with a pressure coefficient of $dE/dP = -38(3)$ meV GPa^{-1} between 0 and 3.2 GPa (represented by the triangles in Fig. 2b). At 4.1 GPa, the emission is no longer observed, evidencing that the band gap becomes indirect. For this reason, the energy values for $P < 3.6$ and $P \geq 3.6$ GPa were extracted by linear extrapolation of $\alpha^2 \times E$ and $\sqrt{\alpha} \times E$ plots, for direct and indirect gaps, respectively (fits shown in Fig. 2b).[57] The abrupt decrease in band gap energy results in a color change in the sample (piezochromism) from bright red in the low-pressure regime ($P < 3.6$ GPa) to dark red in the high-pressure regime, as evidenced by the photographs shown in Fig. 2c.

The experimentally obtained band gap value of 1.99 eV for $HgPSe_3$ under ambient conditions is in good agreement with

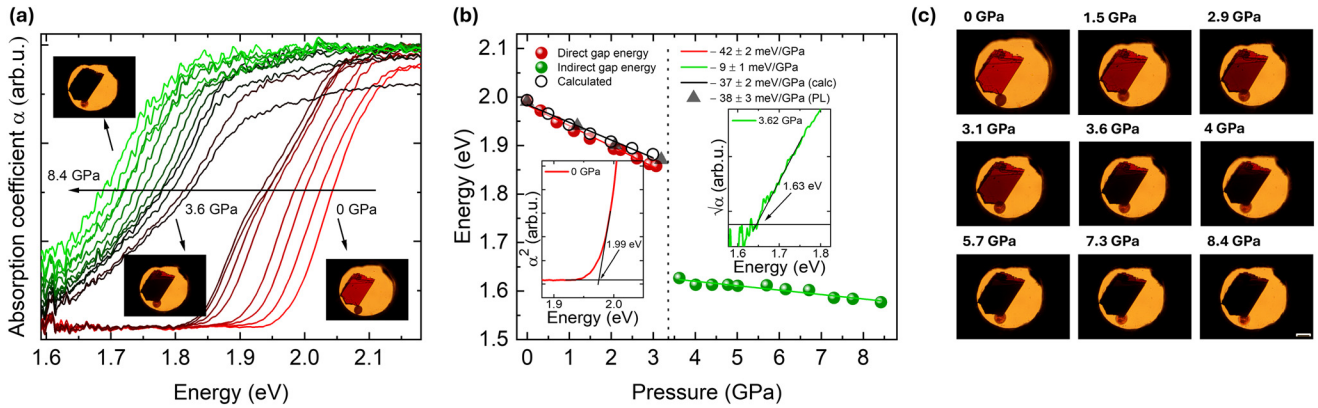

Fig. 2 (a) Evolution of the absorption coefficient with increasing pressure. A phase transition is observed at 3.6 GPa, which is marked by a jump in band gap energy of 0.192 eV, together with color change from bright to dark red, and less steep slopes. The saturation in the absorption spectra arises when the actual transmitted light above the absorption edge is much smaller than the signal coming from scattered light in the DAC rather than from transmission through the sample. (b) Red and green symbols are the experimental values of absorption edge energy at each pressure, with corresponding linear fits. Black circles indicate the theoretical values. Triangles correspond to emission energies acquired from photoluminescence measurements (spectra shown in Fig. S5 (SI)). The slopes of the solid lines represent the pressure coefficients. Insets show examples of Tauc plots of the form $\alpha^2 \times E$ and $\sqrt{\alpha} \times E$ for extracting direct and indirect gap energies, respectively. (c) Optical images of the evolution of the sample color during compression show that the phase transition is accompanied by a sudden darkening. A ruby sphere used for pressure calibration can be seen next to the sample. Scale bar in the last image: 40 μm.

previous results from reflectivity and absorption measurements at room temperature, which yielded 1.95 eV.[17,58] The experimental pressure coefficients obtained from the linear fits of the E–P curves are $dE/dP = -42(2)$ meV GPa^{-1} below the critical pressure of 3.6 GPa, and $dE/dP = -9(1)$ meV GPa^{-1} above it, suggesting that the crystal is more sensitive to pressure in the low-pressure regime, which is expected since the weak van der Waals forces mediating the interlayer interactions strengthen under increasing pressure and decreasing interlayer distances. The theoretical pressure coefficient of $dE/dP = -37(2)$ meV GPa^{-1} obtained from DFT calculations is in good agreement with our experimental values for the low-pressure phase from both absorption and PL measurements. Such band gap shrinkage has also been observed in other compounds in the MPS_3 family, such as $MnPS_3$, in which the band gap was found to systematically decrease from 2.64 eV under ambient conditions to 2.15 at 11.5 GPa, with a rate of approximately −50 meV GPa^{-1}.[59] Such piezochromism was also present, but neither an abrupt change in the absorption edge energy nor a change in slope occurred in the investigated range. Negative pressure coefficients have also been found for the direct fundamental transitions in ReX_2, with values ranging from −14 to −42 meV GPa^{-1}, and −25 meV GPa^{-1} for the indirect fundamental transition of WSe_2, while in group VI MX_2 compounds the direct excitonic transitions were found to have positive pressure coefficients, ranging from approximately 20 to 40 meV GPa^{-1}.[60–62]

The reduction in band gap energy due to increased pressure is in agreement with our band structure calculations up to 3 GPa, shown in Fig. 3. The calculated band structure reveals that the valence band reaches its maximum at the Γ point, whereas the conduction band minimum (CBM) does not coincide with any high-symmetry k-point but instead lies in

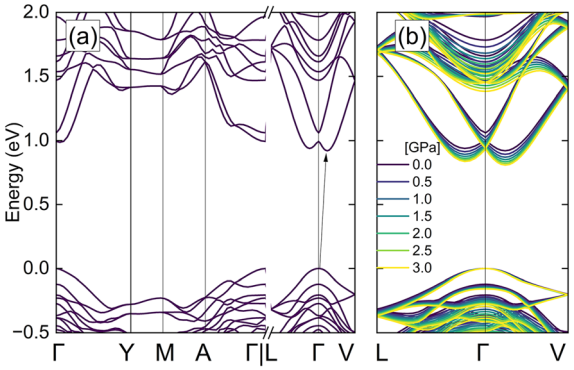

Fig. 3 (a) Electronic band structure of $HgPSe_3$ at 0 GPa and (b) with pressure dependence up to 3 GPa. The arrow indicates the lowest energy (quasi-direct) transition at the Γ k-point. A shrinkage of the fundamental transition (band-gap related) with increasing pressure is evidenced.

the vicinity of Γ along the Γ → V path (see Fig. 3). With increasing pressure, the energy separation between the direct transition at Γ and the indirect Γ → CBM transition increases, indicating that the band gap becomes progressively more indirect; however, this difference remains sufficiently small so that $HgPSe_3$ can still be considered a quasi-direct band-gap material in the entire low-pressure monoclinic phase. This behavior is consistent with the gradual enhancement of interlayer coupling under compression, which modifies the dispersion of both valence and conduction bands. Notably, the conduction band valleys along Γ → V become increasingly sensitive to pressure, which explains the experimentally observed weakening of the quasi-direct character prior to the structural phase transition. Antonatos *et al.*[18] pointed out that such

quasi-direct nature of the band gap of $HgPSe_3$ is responsible for the long decay times, in the order of nanoseconds, observed in time-resolved measurements, and this is due to the reduced momentum overlap between the conduction and valence band states.

3.2 Structural properties

The powder XRD patterns from 0.5 to 8 GPa collected with λ = 0.4246 Å are shown in Fig. 4. It can be seen that, as the pressure increases, peaks start to appear, disappear, merge, or split, suggesting a structural phase transition. With increasing pressure, all peaks shift to higher angles, indicating a reduction of all interplanar distances with increasing pressure, as expected from Bragg's law. The indexed peaks from the 0.5 GPa pattern, labeled in Fig. 5, reproduce the expected lattice parameters obtained by Jandali *et al.*[23] under ambient conditions (see Table 1). Experimental and calculated positions, along with the corresponding Miller indices of such peaks are displayed in Table S1 (SI).

Qualitatively, the first significant change in the diffraction pattern is observed at approximately 3.8 GPa, where a new peak appears at $2\theta \approx 8.5°$, which persists only up to around 5 GPa. Also, two peaks merge into a single peak centered at $2\theta \approx 7.7°$, and at 5 GPa, two peaks emerge near the previously merged peak: one at lower angles at $2\theta \approx 7.6°$, and another at higher angles at $2\theta \approx 7.9°$. The merged peak vanishes at around 6.1 GPa, but the newly emerged peaks persist up to 8 GPa. A profile-matching refinement (Le Bail method) was performed for the 0.5 GPa data using the FullProf software, and the results are shown together with the experimental pattern and the difference profile at the bottom of the plot from Fig. 5.

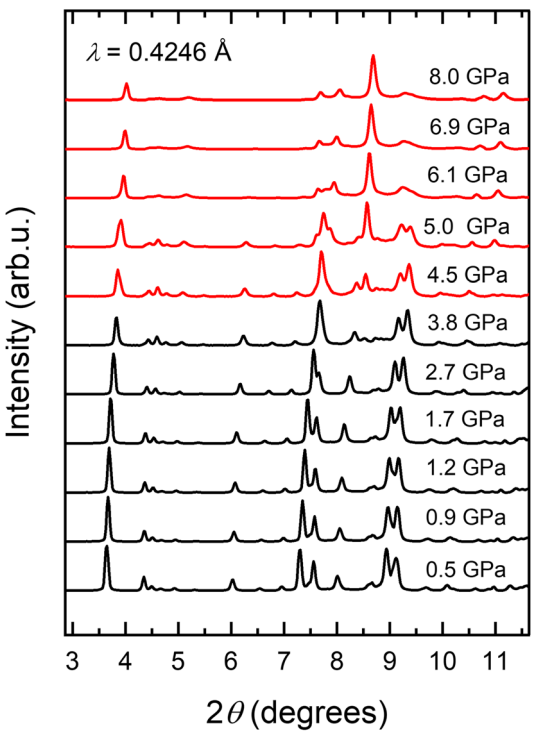

Fig. 4 Selected powder X-ray diffraction pattern of $HgPSe_3$ from 0.5 to 8 GPa collected with λ = 0.4246 Å. Change in color indicates two possible phases: monoclinic (black) up to 3.8 GPa and triclinic (red) from 4.5 GPa.

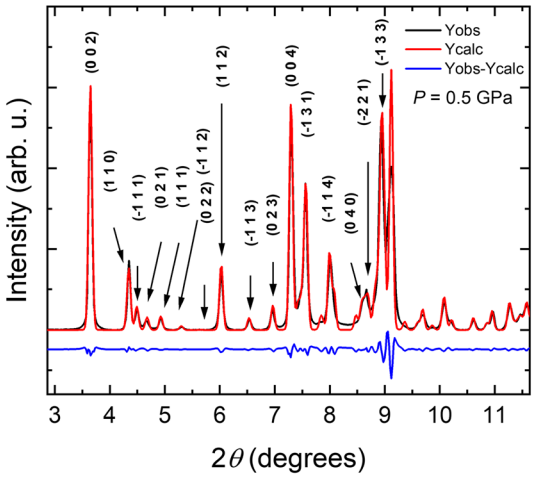

Fig. 5 Le Bail refinement of the 0.5 GPa pattern: black curve is the experimental pattern and the red curve is the refinement fit. The lower blue curve is the difference between the observed and calculated intensities. Corresponding Miller indices of the first 16 peaks are indicated. All diffraction peaks were considered in the refinement.

In order to obtain the pressure dependence of the lattice parameters a, b, c, α, β, γ, the same Le Bail method was employed. The fitting at 5 GPa is shown in Fig. S6 (SI). In addition, a least-square method was used to obtain additional insight into the high-pressure phase. Detailed information on this method can be found in SI. Both methods yielded the same exact parameters, and the results are shown in Fig. 6a and 7. Furthermore, the experimental evolution of a, b, c with pressure is in good agreement with the theoretical predictions performed for the lower pressure phase up to 3 GPa (solid lines from Fig. 6a). The normalized lattice parameters a/a_0, b/b_0, c/c_0 are shown in Fig. 6b as a function of pressure. The corresponding experimental and calculated pressure coefficients of the normalized lattice parameters $(1/a_i)(\mathrm{d}a_i/\mathrm{d}P)$ were obtained and are shown in Table 2. From these, the isothermal compressibility tensor can be calculated. For a monoclinic structure, the nonzero components of the tensor (obtained within the infinitesimal Lagrangian approximation as implemented in EoSFit7c software[63] and referred to the orientation of the Cartesian axis defined by $\boldsymbol{e}_1 \| \boldsymbol{a}^\star$ and $\boldsymbol{e}_3 \| \boldsymbol{c}$) are β_{11} = 6.7(1), β_{22} = 4.2(2), β_{33} = 14.5(2) and $\beta_{13} = \beta_{31}$ = 4.8(2) in units of 10^{-3} GPa^{-1}. The strong compressibility in the $\boldsymbol{e}_3$ direction is a consequence of the large pressure coefficient of c axis, which contributes the most to volume reduction upon compression.

With respect to the lattice angles, we show in Fig. 7 that β changes only slightly under compression below 4 GPa. This suggests that pressure has a minimal effect on the overall shape and symmetry of the monoclinic structure, without causing it to become more orthogonal or distorted. However, a deviation of α and γ from 90° takes place above the transition

Table 1 Comparison of lattice parameters *a*, *b*, *c* and unit cell volume *V* between our simulated and experimental data at 0 and 0.5 GPa, respectively, and previously reported experimental results at ambient pressure. Experimental values at 0.5 GPa were obtained using DICVOL

Pressure	*a* (Å)	*b* (Å)	*c* (Å)	*V* (Å^3)	*β* (°)	Ref.
0 GPa (calculated)	6.559	11.473	13.771	1025.482	98.273	This work
0 GPa (experimental)	6.545	11.377	13.610	1003.4	98.47	23
0.5 GPa (experimental)	6.508(2)	11.336(3)	13.490(4)	983.5(5)	98.45(3)	This work

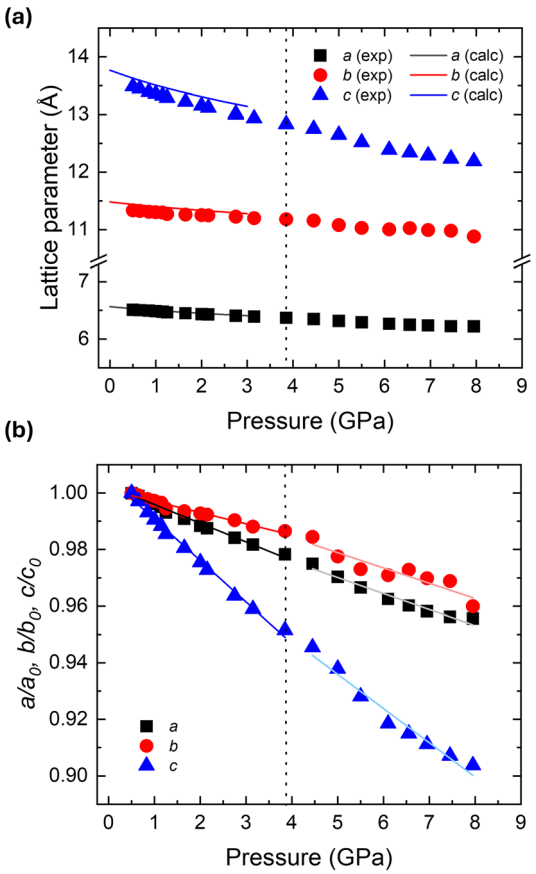

Fig. 6 (a) Evolution of lattice parameters *a*, *b*, *c* with pressure. The solid lines are results from calculations for the low-pressure monoclinic phase up to 3 GPa. (b) Normalized experimental lattice parameters a/a_0, b/b_0, c/c_0 as a function of pressure. Solid lines represent the fits used to determine the pressure coefficients shown in Table 2. Vertical dashed lines indicate the critical pressure of 3.8 GPa.

Table 2 Pressure coefficients of the normalized lattice parameters, $(1/a_i)(da_i/dP)$, for experimental and theoretical data in the low- and high-pressure phases. Units are in10^{-3} GPa^{-1}

Axis *i*	Exp. ≤ 3.8 GPa	Calc. ≤ 3.0 GPa	Exp. > 3.8 GPa
a	−6.6(1)	−7.9(3)	−5.6(5)
b	−4.0(2)	−5.9(2)	−5.4(9)
c	−14.6(4)	−14.9(7)	−12.1(9)

pressure. This result indicates an evolution towards a lower-symmetry triclinic structure, in which none of the angles is equal to 90°. While our fitted model suggests that the high-

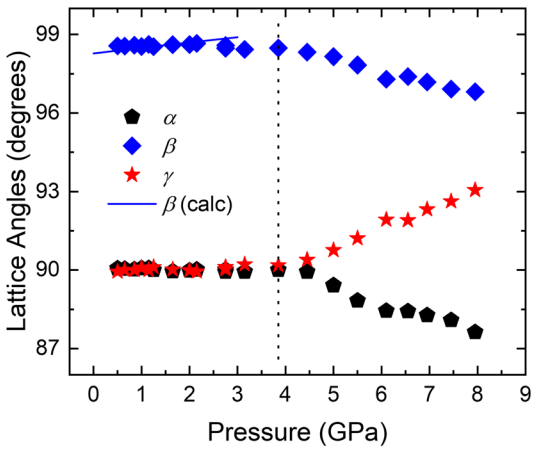

Fig. 7 Experimental lattice angles α, β and γ as a function of pressure, with β also showing calculated values for the low-pressure phase. The deviation of α and γ from 90° near the critical pressure indicates a transition to a lower-symmetry phase.

pressure phase is triclinic, we investigated possible structures using DICVOL software,[44,45] which also found only triclinic solutions above 3.8 GPa. Single-crystal high-pressure measurements would therefore be desirable to elucidate the exact high-pressure structure.

Upon decrease of interatomic distance, monoclinic-to-triclinic transition has been observed in other van der Waals crystals such as VI_3, which goes from the ambient trigonal $R\bar{3}$ structure to monoclinic at approximately 79 K, and then to a triclinic structure upon further cooling.[64] Nevertheless, studies carried out in the magnetic MPS_3 compounds revealed a different trend: in general, at high pressure, they either undergo isostructural phase transition to $C2/m$ symmetry or transition to the trigonal space group, which has higher symmetry than the initial monoclinic $C2/m$ structure. For example, XRD measurements suggested that $MnPS_3$ and $MnPSe_3$ undergo an isostructural transition accompanied by a volume collapse of approximately 20% at around 30 and 25 GPa, respectively.[25] First-principles calculations predicted a structural transition in $MnPS_3$ from initial $C2/m$ to $P\bar{3}1m$ at around 10 GPa, and a transition back to $C2/m$ was expected around 30 GPa.[59] A later experimental work suggested the existence of an isostructural phase transition within the monoclinic system in the range 1–6 GPa, and no further transitions were observed up to the limit of 28 GPa.[65] For $FePS_3$ an isostructural phase transition occurred at 10 GPa, followed by $C2/m \rightarrow P\bar{3}1m$ at 18 GPa.[26] In $NiPS_3$, a $C2/m \rightarrow P\bar{3}$ transition was observed at 13

GPa, followed by subsequent transitions to $P\bar{3}1m$, $P31m$ and finally $P3$ symmetries at 16, 24 and 27 GPa, respectively.[32,66] In $CoPS_3$, a $C2/m \rightarrow P\bar{3}$ transition occurred at 17 GPa.[67] Therefore, $HgPSe_3$ follows a different trend from that observed for other monoclinic compounds of the MPS_3 family.

The experimental and calculated pressure-volume evolution is displayed in Fig. 8, from which we fitted to the low-pressure phase the second-order Birch–Murnaghan isothermal equation of state (BM EoS), given by

$$P(V) = \frac{3}{2}B_0\left[\left(\frac{V_0}{V}\right)^{7/3} - \left(\frac{V_0}{V}\right)^{5/3}\right] \quad (1)$$

to extract the bulk modulus B_0 of $HgPSe_3$.[68] Since the Eulerian strain *versus* normalized pressure relation (shown in the inset of Fig. 8) lies on a constant straight line within experimental error, the experimental data are adequately described by a 2nd-order BM EoS.[69] We obtained B_0 = 29.7(6) and 28.1(5) GPa, and V_0 = 999.9(1) and 1023.5(1) Å^3 from the experimental and calculated data, respectively. In the investigated range of 0–8 GPa, the volume of $HgPSe_3$ evolved from 1003.4 Å^3 to 817.5 Å^3, which corresponds to a volume reduction of 18.5%.

The second-order BM EoS parameters obtained from the fittings are displayed in Table 3, together with experimental bulk moduli for other van der Waals crystals up to 4 GPa. Our results show that the bulk modulus of $HgPSe_3$ is particularly small, comparable to that of WSe_2. In comparison to $MnPSe_3$, $HgPSe_3$ exhibits a significantly smaller bulk modulus and roughly twice larger volume per formula unit. This indicates that the investigated crystal is more compressible, likely due to weaker interlayer interactions.

3.3 Vibrational properties

In order to shed light into the nature of the high-pressure phase and the transition pressure value, pressure-dependent Raman spectroscopy was the technique of choice owing to its well-known high sensitivity to local structure and distortions. Spectra recorded up to 7.4 GPa in hydrostatic conditions are shown in Fig. 9a. Throughout the whole pressure range, the

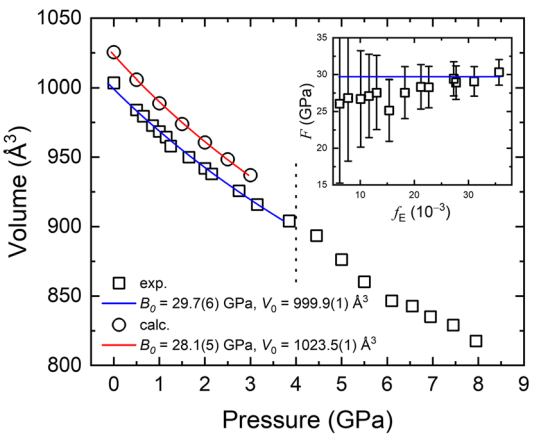

Fig. 8 Volume as a function of pressure of $HgPSe_3$ as obtained by XRD measurements and DFT calculations. The low-pressure phase was fitted using second-order Birch–Murnaghan equation of state, represented by the solid lines. The experimental volume at ambient conditions was taken from ref. 23. The inset shows the normalized pressure *vs.* Eulerian strain ($F - f_E$) plot.

Table 3 Experimental and calculated parameters of the second-order Birch–Murnaghan EoS for $HgPSe_3$, with comparison to reported experimental values for other Se-based van der Waals crystals up to 4 GPa. Unit-cell volumes per formula units (p.f.u.) are shown for direct comparison

Compound	Vol. p.f.u. (Å^3 p.f.u.)	B_0 (GPa)	Ref.
$HgPSe_3$ (exp.)	249.8	29.7(6)	This work
$HgPSe_3$ (calc.)	256.4	28.1(5)	This work
$MnPSe_3$	117.1	35(4)	25
$ReSe_2$	61.9	47(2)	70
$MoSe_2$	60.4	34(4)	71
WSe_2	60.4	30(5)	72

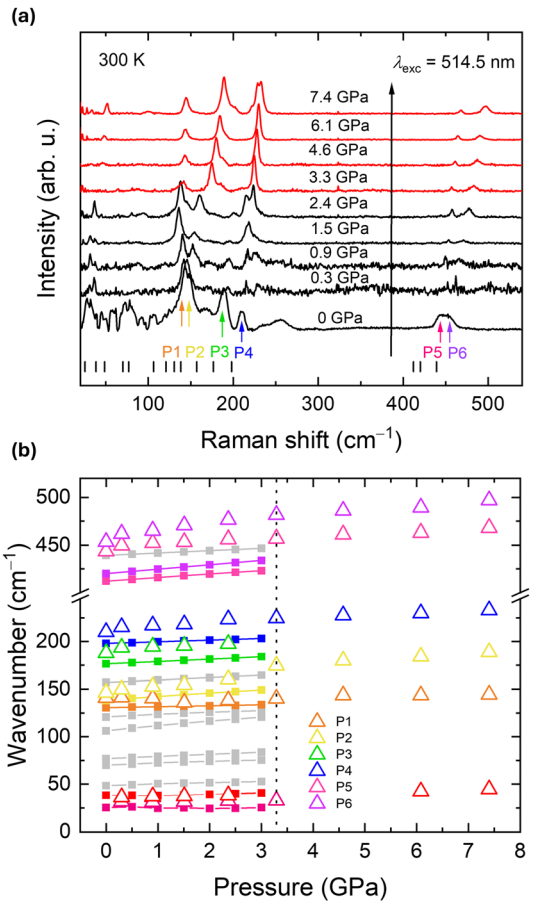

Fig. 9 (a) Pressure-dependent Raman spectra of $HgPSe_3$ acquired with excitation wavelength λ = 514.5 nm. Six main vibrational modes observed experimentally are labeled P1–P6. Two structural phases are evidenced from the number and position of Raman peaks. Spectra is colored accordingly. Transition pressure is 3.3 GPa. Black vertical ticks indicate the calculated phonon frequencies of the A_g modes at 0 GPa. (b) Triangles show experimental peak positions as a function of pressure, while squares and solid lines represent calculated A_g modes from 0 to 3 GPa. Grey colors denote the A_g modes which were not observed experimentally.

peaks lie mostly in the range 100–250 and 400–500 cm^{-1}. The spectral positions and the number of peaks at 0 GPa are in good agreement with previous studies under similar experimental conditions, in which modes were assigned as E_g (peaks at around 149 and 168 cm^{-1}), A_{1g} (peaks at around 212 and 449 cm^{-1}), and Hg–Se vibration (peak at around 192 cm^{-1}).[18] However, these assignments were made under the simplified assumption of the D_{3d} symmetry of the P_2Se_6 units. In contrast, since the structure of $HgPSe_3$ belongs to the C_{2h} point group, the in-plane A_{1g} assignments remain appropriate, but the out-of-plane E_g modes correspond to B_g modes under the C_{2h} symmetry. In the case of $HgPSe_3$ with monoclinic structure and space group $C2/c$, the irreducible representation of the zone-center optical phonon modes is

$$\Gamma(C_{2h}) = 15A_g + 14A_u + 15B_g + 13B_u, \quad (2)$$

where the g modes (gerade) are Raman-active, while the u modes (ungerade) are infrared-active.[73] Since $HgPSe_3$ has an inversion center, none of its modes can be both Raman and infrared-active according to the mutual exclusion rule. Although both A_g and B_g signals are present in the high-pressure measurements, the spectrometer used is more efficient in the parallel-polarization configuration. In addition, A_g modes are intrinsically more intense than B_g modes, as demonstrated by the Raman-polarization measurements shown in Fig. S7 (SI). For these reasons, all Raman peaks presented here are assigned to A_g modes and are compared exclusively with calculated A_g phonons. This assignment represents a reasonable simplification, since our calculations show that the energy difference between corresponding A_g and B_g modes is in the order of 1 cm^{-1}, as displayed in Table S2 (SI).

Six main vibrational modes are observed experimentally at 0 GPa, and they are located at approximately 141.1, 146.7, 187.9, 210.1, 443.6 and 453.6 cm^{-1}, labeled P1–P6 in Fig. 9b. The vibrational frequencies were obtained by fitting the data with Lorentzian functions, and detailed figures showing the peak evolution with pressure are shown in Fig. S8–S10 (SI). Additionally, Raman spectra at ambient conditions with different acquisition times were collected to investigate possible sample degradation due to laser power, and the results are presented in Fig. S11. At 0.3 GPa, peaks P1 and P2 exhibit opposite trends with increasing pressure: the former shifts to lower wavenumbers (*i.e.* it is a soft mode) until 1.5 GPa and then blue shifts at higher pressures, while the latter shifts to larger wavenumbers, with increased intensity after 3.3 GPa. The hardening of the soft mode at 3.3 GPa indicates that a structural transition took place towards a more stable phase. At 0.3 GPa, two low-intensity peaks appear in the low-frequency range (≈30–36 cm^{-1}): those vanish at 3.3 GPa, but for pressures higher than 6.1 GPa the peak at higher wavenumber shows increased intensity. At 2.4 GPa, peak P1 starts to blueshift, and this trend is observed until 7.4 GPa. Peak P2 shifts to higher wavenumbers throughout the entire range, and the shift becomes stronger after 3.3 GPa. Peak P3 slightly shifts toward higher wavenumbers as its intensity decreases, and at 3.3 GPa it can no longer be seen. Peak P4 blue shifts with increasing pressure. At 2.4 GPa, it splits into two peaks, which merge again at 3.3 GPa; the peak then splits again at 7.4 GPa. The blueshift persists over the entire pressure range, accompanied by an increase in intensity. With regard to the Raman features around 450 cm^{-1}, only two peak wavenumbers (peaks P5 and P6) were reliably extracted due to the high signal-to-noise ratio present at pressures below 1.5 GPa. With increasing pressure, these two peaks become clearly visible, showing an increasing spectral separation and a decrease in intensity. We therefore conclude that a structural phase transition occurs between 2.4 and 3.3 GPa, which is lower than the transition pressure obtained from XRD measurements (≈3.8 GPa). This is expected since Raman spectroscopy probes phonons and local bonding symmetry, while XRD probes long-range crystallographic order.[74] Raman modes may split, soften, or shift when local symmetry is lowered, while XRD only shows the transition once the average crystal structure becomes triclinic.[75] Moreover, since the number of Raman peaks at the high-pressure phase does not increase, we propose that the triclinic phase is centrosymmetric (*i.e.* space group $P\bar{1}$ and point group C_i).

From the evolution of phonon frequencies with pressure, shown in Fig. 9b, the pressure coefficients $d\omega/dP$ were determined for both the experimental and the calculated data from linear fits, and the values are shown in Table 4 (low-pressure phase only). Using the bulk modulus B_0 = 29.7 GPa obtained from the XRD analysis, we calculated the Grüneisen parameters γ_i of each peak by using the expression $(B_0/\omega_{i0})d\omega_i/dP$. Except for peak P1 below 2.4 GPa, all modes shift to higher wavenumbers under compression, with γ_i values between approximately 0.3 and 1.1, indicating varying sensitivity to pressure. Remarkably, peak P1 has the lowest pressure coefficient, while peak P6 has the highest. It is worth noting that this trend is consistently observed for both the experimental and calculated values.

The calculated phonon dispersion of bulk $HgPSe_3$ is shown in Fig. 10 together with the phonon density of states (PDOS). Dominating atomic displacements for each vibrational modes are shown in red, violet and green lines for mercury, phosphorus and selenium, respectively. From this classification, it can be seen that low-frequency modes are dominated by

Table 4 Experimental and calculated zero-pressure frequencies (ω_0), phonon pressure coefficients ($d\omega_i/dP$), and mode Grüneisen parameters (γ_i) for the Raman-active modes of the low-pressure phase of $HgPSe_3$. The Grüneisen parameters have been calculated using the bulk modulus B_0 = 29.7 GPa

Symmetry	ω_0^{exp} (cm^{-1})	$(d\omega_i/dP)^{exp}$ (cm^{-1} GPa^{-1})	$\gamma_i^{exp.}$	$\omega_0^{calc.}$ (cm^{-1})	$(d\omega_i/dP)^{calc.}$ (cm^{-1})
A_g (P1)	141.1	−1.8(9)	−0.38	130.58	1.01(3)
A_g (P2)	146.5	5.5(5)	1.12	138.29	3.61(8)
A_g (P3)	188.0	3.6(9)	0.57	176.6	2.49(16)
A_g (P4)	210.1	4.9(9)	0.69	198.03	1.72(14)
A_g (P5)	443.6	4.6(12)	0.31	412.09	3.71(4)
A_g (P6)	453.6	8.9(13)	0.58	420.12	4.630(4)

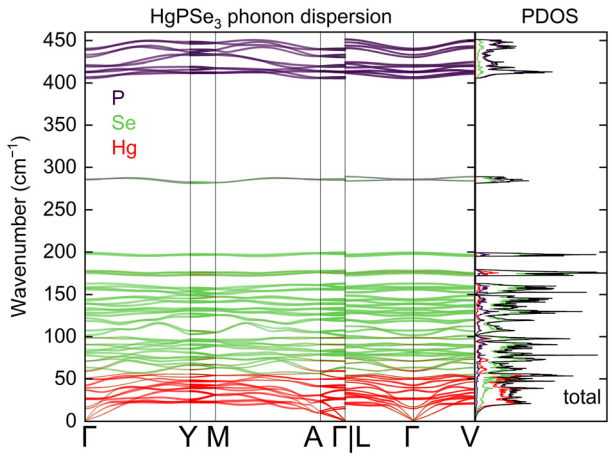

Fig. 10 *Ab initio* calculation of the phonon dispersion curves of bulk $HgPSe_3$. The right panel shows the corresponding phonon density of states (PDOS). Colors represent atomic displacement contribution for each phonon mode, being red, violet and green used for Hg, P and Se, respectively.

vibrations involving mainly the heavy Hg atoms, the mid-frequency region arises mainly from Hg–Se vibrations, while the high-frequency modes originate predominantly from vibrations of the P_2Se_6 units. This partitioning of the vibrational spectrum is consistent with the Raman-active features observed experimentally within an error of 10 cm^{-1}, as indicated by the black vertical ticks in Fig. 9a. Differences between experimental and calculated phonon energies partly arise from the employed PBE exchange–correlation functional. Despite being standard for phonon calculations in layered materials, this functional is known to slightly overestimate lattice parameters, which in turn reduce the interatomic forces and therefore phonon energies. Despite these systematic differences, the overall structure of the phonon spectrum is well reproduced. In particular, the grouping, ordering, and relative spacing of the vibrational branches are faithfully captured by the calculations. These, combined with the calculated pressure coefficients, allowed us to provide an assignment of all experimental Raman features (shown in Table 4).

The visualizations of the Raman-active A_g modes assigned to the experimental spectra (corresponding to peaks P1–P6) are shown in Fig. 11. Hg atoms appear as red, P as purple, and Se as green, with arrows indicating the atomic displacement directions and relative amplitudes. In this wavenumber range, P and Se atoms exhibit the largest vibrational amplitudes, as highlighted by the arrows, while Hg atoms show significantly smaller amplitudes.

Lastly, Raman spectra acquired during decompression confirm the reversibility of the phase transition, as shown in Fig. S2 (SI). Overall, results from all applied techniques (structural, optical, and vibrational) indicate reversible behavior, which is particularly evident in the absorption measurements. The decompression datasets from absorption and XRD measurements are presented in Fig. S1, S3 and S4 (SI).

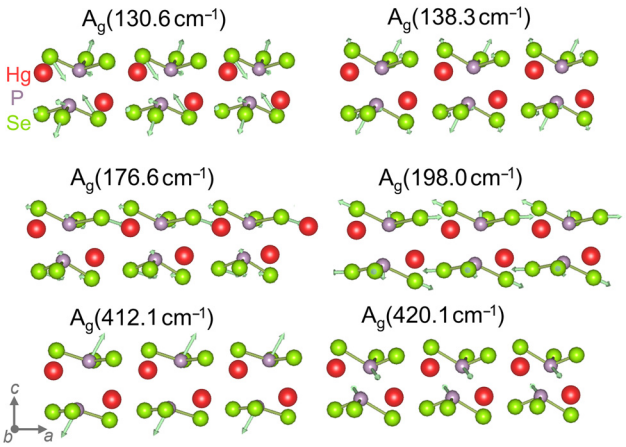

Fig. 11 Visualization of selected A_g phonon modes for bulk $HgPSe_3$ from DFT calculations. Hg atoms appear as red, P atoms as purple, and Se atoms as green. Arrows show atomic displacement and their length scales with displacement amplitude.

4 Conclusions

We report the effect of hydrostatic pressure on the optical, structural, and vibrational properties of layered $HgPSe_3$, and we conclude that a phase transition is present between 2.4 and 3.8 GPa. From absorption spectroscopy, it was found that the absorption edge energy red shifts with an experimental pressure coefficient of $dE/dP = -42(2)$ meV GPa^{-1} below the critical pressure of 3.6 GPa, and then abruptly decreases by nearly 200 meV at this pressure, after which it continues to decrease with rate $dE/dP = -9(1)$ meV GPa^{-1}. The redshift is consequently accompanied by a change in the sample color from the original bright red to dark red. This is in good agreement with band structure calculations which showed that the fundamental transition red shifts with rate $dE/dP = -37(2)$ meV GPa^{-1} in the range 0–3 GPa. The slope of the absorption curves becomes less steep after the transition, evidencing an electronic phase transition from quasi-direct to indirect band gap, confirmed by pressure-dependent photoluminescence measurements.

Our analysis of powder XRD data collected up to 8 GPa indicates that a phase transition from a monoclinic to a triclinic structure starts at 3.8 GPa. The theoretical pressure dependence of the lattice parameters agrees well with the experimental observations. We report an experimental bulk modulus of 29.7 GPa in very good agreement with the theoretical value of 28.1 GPa, obtained with the second-order Birch–Murnaghan EoS fits. Raman scattering measurements confirm that a structural phase transition occurs between ≈2.4 and 3.3 GPa. The Raman peaks were assigned to A_g modes on the basis of theoretical calculations and polarization-resolved Raman spectroscopy. Furthermore, it was observed that all peaks – except one – shift to higher frequencies upon compression. Overall, our results demonstrate a clear pressure-induced redshift and

structural evolution, providing insight into the high-pressure behavior of $HgPSe_3$.

Author contributions

Conceptualization: B. d. S., R. O., N. A., R. K. Investigation: B. d. S., R. O., O. G., P. B., D. E., J. K., F. D., A. K. T. Formal analysis: B. d. S., R. O., M. R. Software: M. R. Resources: I. P., Z. S. Writing – original draft: B. d. S., R. O. Writing – review & editing: N. A., R. K., J. I., P. S., all authors. Supervision: N. A., R. K. All authors have read and agreed to the published version of the manuscript.

Conflicts of interest

The authors declare no conflicts of interest.

Data availability

The data supporting the findings of this study are available within the article and its supplementary information (SI). Supplementary information is available, and it includes decompression data from all experimental techniques, pressure-dependent photoluminescence spectra, as well as detailed description of XRD and Raman analysis along with supplementary plots. See DOI: https://doi.org/10.1039/d5nr05417f.

Additional data are available from the corresponding authors upon reasonable request.

Acknowledgements

B. d. S. acknowledges financial support from Marie Skłodowska-Curie Innovative Training Network (MSCA ITN (GA 956813)) within the Horizon 2020 Programme of the European Commission. N. A. and M. R. acknowledge funding from National Science Centre (NCN) Poland SONATA 19 Grant 2023/51/D/ST11/02588. R. O., J. I., O. G., P. B. and D. E. acknowledge ALBA synchrotron light source for funded experiments under proposals no. 2018093018 and 2023027486 at the BL04-MSPD beamline and support from the beamline scientist Dr Catalin Popescu. Z. S. was supported by ERC-CZ program (project LL2101) from Ministry of Education Youth and Sports (MEYS) and by the project Advanced Functional Nanorobots (reg. no. CZ.02.1.01/0.0/0.0/15_003/0000444 financed by the EFRR). M. R. acknowledges access to the BEM computing cluster provided by the Wroclaw Centre for Networking and Supercomputing (WCSS). P. B. and D. E. thank Generalitat Valenciana (GVA) for the Postdoctoral Fellowship No. CIAPOS/2023/406. This publication is financed by the Spanish Ministerio de Ciencia e Innovación and the Agencia Estatal de Investigación MCIN/AEI/10.13039/501100011033 as part of the project MALTA Consolider Team network (RED2022-134388-T), and I+D+i projects PID2022-138076NB-C41/C42 cofinanced by EU FEDER funds, by projects PROMETEO CIPROM/2021/075 (GREENMAT) and MFA/2022/007 financed by GVA. This study also forms part of the Advanced Materials program supported by MCIN with funding from European Union NextGenerationEU (PRTR-C17.I1) and by GVA through project MFA/2022/025 (ARCANGEL).

References

1 A. K. Geim and K. S. Novoselov, *Nat. Mater.*, 2007, **6**, 183–191.
2 K. F. Mak, C. Lee, J. Hone, J. Shan and T. F. Heinz, *Phys. Rev. Lett.*, 2010, **105**, 136805.
3 K. F. Mak, K. He, J. Shan and T. F. Heinz, *Nat. Nanotechnol.*, 2012, **7**, 494–498.
4 B. Radisavljevic, A. Radenovic, J. Brivio, V. Giacometti and A. Kis, *Nat. Nanotechnol.*, 2011, **6**, 147–150.
5 Q. H. Wang, K. Kalantar-Zadeh, A. Kis, J. N. Coleman and M. S. Strano, *Nat. Nanotechnol.*, 2012, **7**, 699–712.
6 D. Jariwala, V. K. Sangwan, L. J. Lauhon, T. J. Marks and M. C. Hersam, *ACS Nano*, 2014, **8**, 1102–1120.
7 S. Manzeli, D. Ovchinnikov, D. Pasquier, O. V. Yazyev and A. Kis, *Nat. Rev. Mater.*, 2017, **2**, 17033.
8 M. Glazov, A. Arora, A. Chaves and Y. G. Gobato, *MRS Bull.*, 2024, **49**, 899–913.
9 W. Ren, P. Boggild, J. M. Redwing, K. S. Novoselov, L. Sun, Y. Qi, K. Jia, Z. Liu, O. Burton, J. A. Webber, *et al.*, *2D Mater.*, 2025, **13**, 021501.
10 D.-B. Long, H. Zhao, J. Zhang, Y. Lei, Z. Zhou, S. Zhang, Z. Yue, S. Peng and X. Wu, *J. Mater. Sci.*, 2025, **60**, 18561–18594.
11 K.-Z. Du, X.-Z. Wang, Y. Liu, P. Hu, M. I. B. Utama, C. K. Gan, Q. Xiong and C. Kloc, *ACS Nano*, 2015, **10**, 1738–1743.
12 X. Zhang, X. Zhao, D. Wu, Y. Jing and Z. Zhou, *Adv. Sci.*, 2016, **3**, 1600062.
13 Y. Kuzminskii, B. Voronin and N. Redin, *J. Power Sources*, 1995, **55**, 133–141.
14 C.-F. Du, Q. Liang, R. Dangol, J. Zhao, H. Ren, S. Madhavi and Q. Yan, *Nano-Micro Lett.*, 2018, **10**, 22.
15 J. Chu, F. Wang, L. Yin, L. Lei, C. Yan, F. Wang, Y. Wen, Z. Wang, C. Jiang, L. Feng, J. Xiong, Y. Li and J. He, *Adv. Funct. Mater.*, 2017, **27**, 1701342.
16 K. Synnatschke, J. van Dinter, A. Müller, D. Tiede, L. Spillecke, S. Shao, D. Kelly, J. Konecny, B. Konkena, M. McCrystall, N. Saigal, U. Wurstbauer, W. Bensch, Z. Sofer, J. N. Coleman, R. Klingeler, S. J. Haigh and C. Backes, *2D Mater.*, 2023, **10**, 024003.
17 L. Liao, E. Kovalska, V. Mazanek, L. Valdman, L. Dekanovský, W. Bing, D. Sedmidubský, J. Luxa, Š. Huber, A. P. Herman, R. Kudrawiec and Z. Sofer, *J. Mater. Chem. C*, 2022, **10**, 8834–8844.
18 N. Antonatos, A. P. Herman, B. de Simoni, K. Ciesiołkiewicz, E. Belas, M. Betušiak, R. Grill,

K. J. Sarkar, A. Subramani, D. Sedmidubský, V. Jadriško, A. Baserga, M. Bertolotti, S. Dal Conte, C. Gadermaier, G. Cerullo, A. Treglia, A. Petrozza, R. Kudrawiec and Z. Sofer, *Nano Lett.*, 2025, **25**, 3053–3058.

19 A. Wiedenmann, J. Rossat-Mignod, A. Louisy, R. Brec and J. Rouxel, *Solid State Commun.*, 1981, **40**, 1067–1072.

20 W. Klingen, R. Ott and H. Hahn, *Z. Anorg. Allg. Chem.*, 1973, **396**, 271–278.

21 E. Prouzet, G. Ouvrard and R. Brec, *Mater. Res. Bull.*, 1986, **21**, 195–200.

22 G. Ouvrard, R. Brec and J. Rouxel, *Mater. Res. Bull.*, 1985, **20**, 1181–1189.

23 M. Z. Jandali, G. Eulenberger and H. Hahn, *Z. Anorg. Allg. Chem.*, 1978, **447**, 105–118.

24 R. Brec, G. Ouvrard, A. Louisy and J. Rouxel, *Ann. Chim.*, 1980, **5**, 499–512.

25 Y. Wang, Z. Zhou, T. Wen, Y. Zhou, N. Li, F. Han, Y. Xiao, P. Chow, J. Sun, M. Pravica, A. L. Cornelius, W. Yang and Y. Zhao, *J. Am. Chem. Soc.*, 2016, **138**, 15751–15757.

26 C. Haines, M. Coak, A. Wildes, G. Lampronti, C. Liu, P. Nahai-Williamson, H. Hamidov, D. Daisenberger and S. Saxena, *Phys. Rev. Lett.*, 2018, **121**, 266801.

27 Y. Wang, J. Ying, Z. Zhou, J. Sun, T. Wen, Y. Zhou, N. Li, Q. Zhang, F. Han, Y. Xiao, P. Chow, W. Yang, V. V. Struzhkin, Y. Zhao and H.-k. Mao, *Nat. Commun.*, 2018, **9**, 1914.

28 M. J. Coak, S. Son, D. Daisenberger, H. Hamidov, C. R. S. Haines, P. L. Alireza, A. R. Wildes, C. Liu, S. S. Saxena and J.-G. Park, *npj Quantum Mater.*, 2019, **4**, 38.

29 M. J. Coak, D. M. Jarvis, H. Hamidov, C. R. S. Haines, P. L. Alireza, C. Liu, S. Son, I. Hwang, G. I. Lampronti, D. Daisenberger, P. Nahai-Williamson, A. R. Wildes, S. S. Saxena and J.-G. Park, *J. Phys.: Condens. Matter*, 2019, **32**, 124003.

30 R. A. Evarestov and A. Kuzmin, *J. Comput. Chem.*, 2020, **41**, 1337–1344.

31 H.-S. Kim, K. Haule and D. Vanderbilt, *Phys. Rev. Lett.*, 2019, **123**, 236401.

32 X. Ma, Y. Wang, Y. Yin, B. Yue, J. Dai, J. Cheng, J. Ji, F. Jin, F. Hong, J.-T. Wang, Q. Zhang and X. Yu, *Sci. China: Phys., Mech. Astron.*, 2021, **64**, 297011.

33 L. Fu, Y. Wan, N. Tang, Y.-m. Ding, J. Gao, J. Yu, H. Guan, K. Zhang, W. Wang, C. Zhang, J.-j. Shi, X. Wu, S.-F. Shi, W. Ge, L. Dai and B. Shen, *Sci. Adv.*, 2017, **3**, e1700162.

34 D. Errandonea, F. J. Manjón, J. Pellicer, A. Segura and V. Muñoz, *Phys. Status Solidi B*, 1999, **211**, 33–38.

35 R. A. Susilo, B. G. Jang, J. Feng, Q. Du, Z. Yan, H. Dong, M. Yuan, C. Petrovic, J. H. Shim, D. Y. Kim and B. Chen, *npj Quantum Mater.*, 2020, **5**, 58.

36 T. Suski and W. Paul, *High Pressure in Semiconductor Physics II, Semiconductors and Semimetals*, Academic Press, San Diego, 1998, vol. 1998.

37 F. Wang, T. A. Shifa, P. Yu, P. He, Y. Liu, F. Wang, Z. Wang, X. Zhan, X. Lou, F. Xia and J. He, *Adv. Funct. Mater.*, 2018, **28**, 1802151.

38 K. Momma and F. Izumi, *J. Appl. Crystallogr.*, 2011, **44**, 1272–1276.

39 G. J. Piermarini, S. Block, J. D. Barnett and R. A. Forman, *J. Appl. Phys.*, 1975, **46**, 2774–2780.

40 C. Stan, C. Beavers, M. Kunz and N. Tamura, *Quantum Beam Sci.*, 2018, **2**, 4.

41 F. Fauth, I. Peral, C. Popescu and M. Knapp, *Powder Diffr.*, 2013, **28**, S360–S370.

42 A. Dewaele, P. Loubeyre and M. Mezouar, *Phys. Rev. B: Condens. Matter Mater. Phys.*, 2004, **70**, 094112.

43 C. Prescher and V. B. Prakapenka, *High Pressure Res.*, 2015, **35**, 223–230.

44 A. Boultif and D. Louër, *J. Appl. Crystallogr.*, 2004, **37**, 724–731.

45 D. Louër and A. Boultif, *Powder Diffr.*, 2014, **29**, S7–S12.

46 J. Rodriguez-Carvajal, J. Gonzalez-Platas and N. A. Katcho, *Acta Crystallogr., Sect. B: Struct. Sci., Cryst. Eng. Mater.*, 2025, **81**, 302–317.

47 S. Klotz, J.-C. Chervin, P. Munsch and G. L. Marchand, *J. Phys. D: Appl. Phys.*, 2009, **42**, 075413.

48 J. Kresse and G. Furthmüller, *Comput. Mater. Sci.*, 1996, **6**, 15–50.

49 N. A. W. Holzwarth, A. R. Tackett and G. E. Matthews, *Comput. Phys. Commun.*, 2001, **135**, 329–347.

50 J. Paier, R. Hirschl, M. Marsman and G. Kresse, *J. Chem. Phys.*, 2005, **122**, 234102.

51 J. D. Monkhorst and H. J. Pack, *Phys. Rev. B*, 1976, **13**, 5188–5192.

52 S. G. L. Grimme and S. Ehrlich, *J. Comput. Chem.*, 2011, **32**, 1456–1465.

53 X. Wu, D. Vanderbilt and D. R. Hamann, *Phys. Rev. B: Condens. Matter Mater. Phys.*, 2005, **72**, 035105.

54 K. Parlinski, Z. Q. Li and Y. Kawazoe, *Phys. Rev. Lett.*, 1997, **78**, 4063–4066.

55 A. Togo, *J. Phys. Soc. Jpn.*, 2023, **92**, 012001.

56 K. Z. Rushchanskii, Y. M. Vysochanskii, V. B. Cajipe and X. Bourdon, *Phys. Rev. B: Condens. Matter Mater. Phys.*, 2006, **73**, 115115.

57 J. Tauc, R. Grigorovici and A. Vancu, *Phys. Status Solidi B*, 1966, **15**, 627–637.

58 C. Calareso, V. Grasso, F. Neri and L. Silipigni, *J. Phys.: Condens. Matter*, 1997, **9**, 4791–4799.

59 N. C. Harms, H.-S. Kim, A. J. Clune, K. A. Smith, K. R. O'Neal, A. V. Haglund, D. G. Mandrus, Z. Liu, K. Haule, D. Vanderbilt and J. L. Musfeldt, *npj Quantum Mater.*, 2020, **5**, 56.

60 F. Dybała, M. P. Polak, J. Kopaczek, P. Scharoch, K. Wu, S. Tongay and R. Kudrawiec, *Sci. Rep.*, 2016, **6**, 26663.

61 P. Shen, X. Ma, Z. Guan, Q. Li, H. Zhang, R. Liu, B. Liu, X. Yang, Q. Dong, T. Cui and B. Liu, *J. Phys. Chem. C*, 2017, **121**, 26019–26026.

62 R. Oliva, M. Laurien, F. Dybala, J. Kopaczek, Y. Qin, S. Tongay, O. Rubel and R. Kudrawiec, *npj 2D Mater. Appl.*, 2019, **3**, 20.

63 R. J. Angel, M. Alvaro and J. Gonzalez-Platas, *Z. Kristallogr. – Cryst. Mater.*, 2014, **229**, 405–419.

64 P. Doležal, M. Kratochvílová, V. Holý, P. Čermák, V. Sechovský, M. Dušek, M. Míšek, T. Chakraborty, Y. Noda, S. Son and J.-G. Park, *Phys. Rev. Mater.*, 2019, **3**, 121401.
65 D. P. Kozlenko, O. N. Lis, N. T. Dang, M. Coak, J.-G. Park, E. V. Lukin, S. E. Kichanov, N. O. Golosova, I. Y. Zel and B. N. Savenko, *Phys. Rev. Mater.*, 2024, **8**, 024402.
66 N. C. Harms, T. Matsuoka, S. Samanta, A. J. Clune, K. A. Smith, A. V. Haglund, E. Feng, H. Cao, J. S. Smith, D. G. Mandrus, H.-S. Kim, Z. Liu and J. L. Musfeldt, *npj 2D Mater. Appl.*, 2022, **6**, 40.
67 T. Matsuoka, R. Rao, M. A. Susner, B. S. Conner, D. Zhang and D. Mandrus, *Phys. Rev. B: Condens. Matter Mater. Phys.*, 2023, **107**, 165125.
68 F. Birch, *Phys. Rev.*, 1947, **71**, 809–824.
69 R. J. Angel, *Rev. Mineral. Geochem.*, 2000, **41**, 35–59.
70 Y.-C. Kao, T. Huang, D.-Y. Lin, Y.-S. Huang, K.-K. Tiong, H.-Y. Lee, J.-M. Lin, H.-S. Sheu and C.-M. Lin, *J. Chem. Phys.*, 2012, **137**, 024509.
71 Z. Zhao, H. Zhang, H. Yuan, S. Wang, Y. Lin, Q. Zeng, G. Xu, Z. Liu, G. K. Solanki, K. D. Patel, Y. Cui, H. Y. Hwang and W. L. Mao, *Nat. Commun.*, 2015, **6**, 7312.
72 E. Selvi, R. Aksoy, R. Knudson and Y. Ma, *J. Phys. Chem. Solids*, 2008, **69**, 2311–2314.
73 W. Brockner and U. Pátzmann, *Z. Naturforsch., A: Phys. Sci.*, 1987, **42**, 517–518.
74 E. Flores, P. Novak and E. J. Berg, *Front. Energy Res.*, 2018, **6**, 82.
75 C.-P. Wang, S. R. Shieh, A. C. Withers, X. Liu, D. Zhang, S. N. Tkachev, A.-E. Djirar, T. Xie and J. D. Rumney, *Sci. Rep.*, 2020, **10**, 63202.